Materials Advances

ROYAL SOCIETY OF CHEMISTRY

PAPER

View Article Online
View Journal | View Issue

Cite this: *Mater. Adv.*, 2024, 5, 1960

Novel chemically reduced cobalt-doped g-C_3N_4 (CoCN-*x*) as a highly heterogeneous catalyst for the super-degradation of organic dyes *via* peroxymonosulfate activation

Aboubakr Ben Hamou, †*[a] Mohamed Enneiymy, †*[b] Salaheddine Farsad,[a] Asma Amjlef,[a] Ayoub Chaoui,[a] Nisrine Nouj,[a] Ali Majdoub,[d] Amane Jada,*[bc] Mohamed Ez-zahery[a] and Noureddine El Alem*[a]

This work presents a novel approach for the design and the stabilization of cobalt oxide nanoparticles supported on g-C_3N_4 (CoCN-*x*) catalyst to efficiently degrade various organic pollutants through peroxymonosulfate (PMS) activation. The catalyst support synthesis process involved a two-step thermal treatment of urea, resulting in high-purity g-C_3N_4 material, confirmed by XPS, ^{13}C NMR, and TGA analyses. Two cobalt oxide NP-based catalysts, CoO and α-$Co(OH)_2$, were then prepared by depositing the cobalt nanoparticles on the g-C_3N_4 support using gas-phase reduction by H_2 (CoCN–H_2) and liquid-phase reduction by $NaBH_4$ (CoCN–$NaBH_4$), respectively. The prepared CoCN-*x* materials were characterized using several techniques, such as FTIR spectroscopy, XRD, TEM, and SEM-EDS, which evidenced that the cobalt oxides were successfully introduced into g-C_3N_4. The effectiveness of the prepared catalysts in degrading organic contaminants was evaluated by activating PMS to generate reactive oxygen species (ROSs), $^1O_2$, $SO_4^{\bullet-}$, $O_2^{\bullet-}$, and $HO^{\bullet}$, as confirmed through quenching experiments and electron paramagnetic resonance (EPR) analysis. These ROSs were responsible for the oxidation of the target contaminants, thereby promoting their mineralization. The results showed that both catalysts, CoCN–$NaBH_4$ and CoCN–H_2, exhibited high catalytic activity throughout a wide pH spectrum, achieving hence complete degradation yields for various organic dyes, including OG, MO, BM, and RhB.

Received 7th October 2023,
Accepted 4th January 2024

DOI: 10.1039/d3ma00818e

rsc.li/materials-advances

1. Introduction

Undoubtedly, the issue of organic dye pollution is becoming an increasing environmental hazard.[1–3] Such pollution results from the intensive development of chemical industries, which is the primary culprit behind the environmental degradation by organic dye pollutants.[4–8] In the last few years, numerous scientific papers have been published with the aim of finding solutions to this environmental contamination problem.[9–16] Despite this vast scientific production, researchers in the field are still not satisfied with the results.[17,18] Further, several solutions were proposed aiming to improve either the process or the material used in the polluted water treatment.[19,20] On the other hand, the inefficiency of the conventional methods in treating dye polluted water makes the discovery of new, less expensive treatment methods with potential industrial application an urgent matter for scientists worldwide.[21–24]

Therefore, the activation of peroxymonosulfate (PMS) or persulfate (PS) by functional catalysts has been identified as a promising solution to the water pollution issue.[25,26] This method, known as sulfate radical-based advanced oxidation processes (SR-AOPs), leads to the production of reactive oxygen radicals and it has undergone extensive research and development. It should be noted that the SR-AOP method has notable advantages including a large operational pH domain, high efficacy, and long-lasting performance.[27,28] Hence, several researchers have investigated the industrial applicability of AOPs based on PMS activation and they have delved into the theoretical and reaction mechanism aspects.[29,30] In essence, the activation process of PMS involves mixing an appropriate catalyst with peroxymonosulfate (PMS) under well-defined operating conditions (temperature, pH, time, concentration, *etc.*)

[a] *Laboratory of Materials and Environment, Ibn Zohr University, Agadir, 80000, Morocco. E-mail: aboubakrben96@gmail.com, n.elalem@uiz.ac.ma*
[b] *Institute of Materials Science of Mulhouse (IS2M-CNRS-UHA), Haute Alsace University, Mulhouse, 68100, France. E-mail: mohamed.enneiymy@gmail.com, amane.jada@uha.fr*
[c] *Strasbourg University, Strasbourg, 67081, France*
[d] *Processes, Materials and Environment Laboratory (LPME), Department of Chemistry, Faculty of Sciences and Technology of Fez, Sidi Mohamed Ben Abdellah University, B.P. 2202, Fez, Morocco*
† These authors equally contribute to this manuscript.

and leads to the generation of free radicals (*e.g.*, $SO_4^{\bullet -}$, $E^{\circ}(SO_4^{\bullet -}/SO_4^{2-})$ = 2.5–3.1 V; $HO^{\bullet}$, $E^{\circ}(HO^{\bullet}/H_2O)$ = 1.9–2.7 V) and/or non-radical species (singlet oxygen, $^1O_2$) through a Fenton-like reaction process. However, the efficacy of radical oxidation reaction, which is a potent method for water treatment, may be impeded by inhibitory agents, including carbonate and chloride ions.[31] Non-radical oxidation, on the other hand, exhibits lower reactivity compared to radical oxidation. However, it possesses superior anti-interference properties, flexibility, and selectivity, making it a reliable choice in practical situations.[32] The control of radical and non-radical degradation mechanisms is crucial for managing the target organic contaminants in various treatment situations due to the notable variations in the nature and concentration of contaminants in aquatic systems.

Over the past decade, researchers have been focusing on two crucial aspects dealing with reactions based on SR-AOPs. The first is the development of stable, well-dispersed metal nanocatalysts in aqueous media that are effective in preventing possible secondary pollution caused by metal leaching during the heterogeneous Fenton-like reactions.[33] In this regard, cobalt has proven to be the most efficient non-noble element for PMS activation, compared to copper, iron, and manganese.[31,34–37] Secondly, in an effort to solve the aspects mentioned above, it has been proposed that immobilizing, and homogeneously dispersing cobalt nanoparticles in 2D materials such as g-C_3N_4,[38] carbon nanotubes,[39] and graphene[40] could be considered as a potential solution. One of the 2D materials used for this purpose is graphitic carbon nitride (g-C_3N_4), which is rich in nitrogen and offers several advantages, such as metal-free nature, excellent thermal and chemical stability, unique adjustable electronic structure, abundance, and cost-effectiveness.[41–44] Table 1 shows various cases of seminal research collection that have served as inspiration sources for our current investigation. Such seminal research collection leads to final observations according to which the use of different cobalt oxide species doped with g-C_3N_4 gives highly effective activators of PMS. To our knowledge, until today there is no available report on the use of α-$Co(OH)_2$ doped g-C_3N_4 composites as catalysts for PMS activation.

The current paper aims at designing new cobalt-based catalysts by using innovative synthesis techniques and mitigating the cobalt nanoparticles' secondary environmental impact occurring during the heterogeneous catalysis. Specifically, two distinct chemical reduction pathways were employed, namely, gas-phase and liquid-phase methods, using H_2 and $NaBH_4$ as reducing agents, respectively. Meanwhile, g-C_3N_4 was explored as a platform for immobilizing these cobalt nanoparticles. Prior to their use, all the CoCN-*x* catalysts were characterized by various techniques. Thereafter, we studied the effectiveness of the constructed CoCN-*x* to catalyze PMS in order to convert various organic dyes into innocuous compounds such as H_2O and CO_2. Finally, the catalytic mechanisms underlying the PMS activation process were systematically studied on various constructed catalysts. Moreover, the ROS identification was accomplished by performing radical scavenger experiments

Table 1 Statistics of related studies about cobalt-doped g-C_3N_4 based catalysts on PMS activation for organic contaminant degradation

Catalyst	Pollutants	Experimental marks	Maximum elimination	Ref.
Cobalt doped g-C_3N_4	4-Chlorophenol (4-CP)	[Catalyst] = 1.0 g L^{-1}; [PMS] = 2.5 mM; pH = 6.3; [4-CP] = 50 mg L^{-1}	100% of 4-CP removal in 90 min.	69
Co-g-C_3N_4	Rhodamine B (RhB)	[Catalyst] = 0.4 g L^{-1}; [PMS] = 0.12 mM; [RhB] = 10.0 mg L^{-1}; pH of RhB = 4.68; under visible light	100% of RhB removal in 25 min.	50
MCOCN-CA	Trichloroethylene (TCE)	[Catalyst] = 0.3 g L^{-1}; [PMS] = 1 mM; TCE = 4 mg L^{-1}	95% of TCE removal in 20 min.	70
$CoMoO_4$-Fe-g-C_3N_4	Methylene blue (MB)	[Catalyst] = 0.1 g L^{-1}; [PMS] = 1.0 mM; [MB] = 50 mg L^{-1}	100% of MB removal in 90 min.	71
Co-doped g-C_3N_4-T	Acid orange 7 (AO7)	[Catalyst] = 0.2 g L^{-1}; [PMS] = 0.5 mM; [AO7] = 10 mg L^{-1}; pH = 7.0	93% of AO7 removal in 30 min.	72
CoO_x@C/g-C_3N_4	Rhodamine B (RhB), methyl orange (MO), methylene blue (MB) and phenol	[Catalyst] = 0.2 g L^{-1}; [PMS] = 0.2g L^{-1}; [pollutant] = 10 mg L^{-1}; under visible light.	Removal of (RhB, 98.1%), (MO, 97.9%), (MO, 99.1%), and (MB, 98.4%) in 10 min	73
Co-CN	Tetracycline (TC)	[Catalyst] = 0.5 g L^{-1}; [PMS] = 0.8 mM; [TC] = 10 mg L^{-1}; pH = 6.9	99.3% of TC removal in 24 min	74
Co_3O_4/g-C_3N_4	Atrazine	[Catalyst] = 0.5 g L^{-1}; [PMS] = 1 mM; [Atrazine] = 50 μM; pH = 7.0; Under visible irradiation	78.5% of Atrazine removal in 35 min	75
Co_3O_4-C_3N_4	Phenanthrene (PHE)	[Catalyst] = 0.3 g L^{-1}; [PMS] = 0.5 g L^{-1}; [PHE] = 1 mg L^{-1}; pH = 7.0	100% of PHE removal in 15 min	76
CN-$CoFe_2O_4$-7	Rhodamine B	[catalyst] = 0.4 g L^{-1}; [PMS] = 0.09 g L^{-1}; [RhB] = 10 mg L^{-1}	50% of RhB removal in 30 min	77
$CoWO_4$/g-C_3N_4	Tetracycline hydrochloride (TCH)	[Catalyst] = 0.04 g L^{-1}; [PMS] = 3 mM; [TCH] = 20 mg L^{-1}	73.7% of TCH removal in 10 min	78
CoCN–$NaBH_4$($Co(OH)_2$-g-C_3N_4)	Orange G (OG), Rhodamine B (RhB), methyl orange (MO), methylene blue (MB)	[Catalyst] = 0.1 g L^{-1}; [PMS] = 0.33 mM; [OG] = 100 mg L^{-1}; [RhB] = [MO] = [MB] = 30 mg L^{-1}	100% removal of (2 min, OG), (3 min, MO), (5 min, RhB), and (6 min, MB)	This work
CoCN–H_2(CoO-g-C_3N_4)	Orange G (OG)		100% of OG removal in 6 min	

and Electron Paramagnetic Resonance (EPR) analysis, wherein it was found that generating non-radical species ($^1O_2$) is the predominant pathway. To achieve this, Orange G was used as a model pollutant in our study.

2. Experimental

2.1. Chemicals and reagents

All chemicals were of analytical grade and used as received without further purification. Urea (CH_4N_2O), and sodium borohydride ($NaBH_4$) were purchased from Merck. Cobalt nitrate $Co(NO_3)_2$ $6H_2O$, ethanol (EtOH), methanol (MeOH), *tert*-butyl alcohol (TBA), L-histidine, *p*-benzoquinone (*p*-BQ), orange G (OG), methyl orange (MO), methylene blue (MB), and potassium peroxymonosulfate ($2KHSO_5{\cdot}KHSO_4{\cdot}K_2SO_4$) available as OXONE® were purchased from Sigma Aldrich. All aqueous solutions were prepared with distilled water.

2.2. g-C_3N_4 preparation

Modified g-C_3N_4 nano sheets were first prepared, according to literature procedures.[42] Thus, as shown in Scheme 1, 10 g of urea was placed within a crucible, which was afterwards covered. The powder underwent calcination at 550 °C for 4 h, with a gradual increase in temperature occurring at a rate of 2.5 °C min^{-1}. The collected material was transferred and deposited into an open crucible. Following that, it was exposed to further heating at 500 °C for a duration of 2 hours, with a gradual ramp rate of 5 °C per minute. Next, after numerous washings with distilled water to eliminate alkaline components, especially ammonia, the brownish powder was dried for 12 h in a vacuum oven maintained at 60 °C. Afterwards the resulting sample was exfoliated through ultra-sonication to obtain g-C_3N_4 nano sheets. The final g-C_3N_4 nano sheet sample was then collected, washed and dried in an oven.

2.3. CoCN-*x* preparation

2.3.1. CoCN–$NaBH_4$. In a beaker, 100 mg of g-C_3N_4 and 40 ml of distilled water were introduced, and the obtained aqueous solution was ultra-sonicated for 30 min, after which 150 mg of cobalt nitrate hexahydrate ($Co(NO_3)_2{\cdot}6H_2O$) was introduced. Then the resulting mixture was put in an ultrasonic bath for 25 min, and then left under stirring for 30 min at room temperature. Then, in order to start the cobalt ion reduction reaction, volumes of $NaBH_4$ (2 M) aqueous solution were introduced gradually to the ($Co(NO_3)_2{\cdot}6H_2O$)/g-C_3N_4 suspension while being stirred for 2 h at 30 °C. The produced nanocomposite was then filtered, and washed with ethanol and distilled water to remove all unnecessary impurities. Finally, the powder was subjected to drying for 24 h in an oven at 60 °C, to get a black magnetic powder, which will henceforth be referred to as CoCN–$NaBH_4$ in this study.

2.3.2. CoCN–H_2. In a beaker, 100 mg of g-C_3N_4 is introduced into 10 ml of ethanol (EtOH) to which is added an amount (150 mg) of cobalt nitrate hexahydrate ($Co(NO_3)_2{\cdot}6H_2O$). The mixture was then stirred for 8–10 h under the hood, until the ethanol was completely evaporated, leading to a powder, which was placed in an oven for 12 h. The resulting powder was again placed in a tubular oven and treated under a gaseous inert mixture of (H_2/Ar) (33%/66%) with a flow rate of 12 L h^{-1} at 300 °C for 4 h with a temperature rise of 5 °C min^{-1}, in order to get a black magnetic powder, which will be denoted in this work as CoCN–H_2. Scheme 1 summarizes the chemical reduction procedures applied for the preparation of used catalysts.

3. Characterization methods

The g-C_3N_4, CoCN–$NaBH_4$, and CoCN–H_2 surface morphologies and microstructures were explored using Scanning Electron

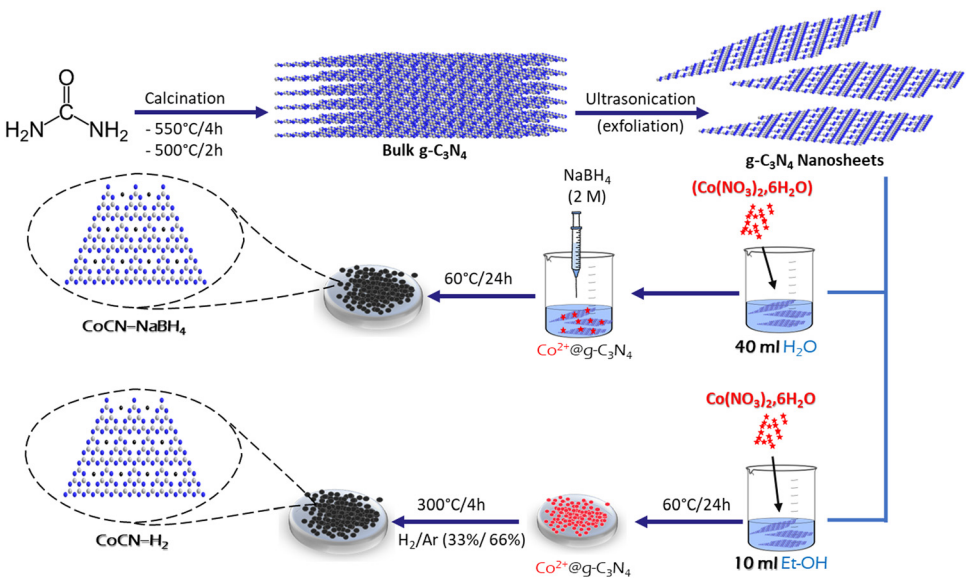

Scheme 1 Schematic diagram of chemical reduction pathways employed for CoCN–$NaBH_4$ and CoCN–H_2 preparation.

Microscopy (SEM, JEOL JSM IT-100) and Transmission Electron Microscopy (TEM, Philips CM 200). Additionally, an Energy Dispersive X-ray (EDX) spectrometry mapping analyzer sensor was linked to the SEM to enhance the analysis and to assess the samples' chemical element compositions. The Fourier transform infrared (FTIR) spectra of the g-C_3N_4, CoCN–$NaBH_4$, and CoCN–H_2 catalysts were obtained by using a SHIMADZU IRAffinity-1S instrument, whereby 1% of the sample was finely ground and subsequently pressed with 99% KBr. The g-C_3N_4 surface chemical analysis was performed by X-ray photoelectron spectroscopy (XPS) (VG SCIENTA, SES-200). The solid-state ^{13}C NMR spectrum of g-C_3N_4 was acquired utilizing the method of cross-polarization magic angle spinning (CP-MAS). The experiments were conducted at room temperature with a 4-mm MAS probe in a Bruker Avance III-600. A Q500 model (TA Instrument) was utilized to conduct thermogravimetric analysis (TGA) of g-C_3N_4. In this analysis, approximately 50 mg of the sample was subjected to a heating process from 25 to 1000 °C at a rate of heating of 5 °C min^{-1} in an environment of air flowing at a rate of 90 mL min^{-1}. Finally, nitrogen adsorption and desorption isotherm analyses were conducted through an AUTOSORB-1 instrument to measure the surface area (S_{BET}) and the pore distribution of the g-C_3N_4.

4. Catalytic activity procedures

The efficiency of catalysts has been evaluated through the assessment of the OG elimination degree upon the PMS activation occurring in the catalyst/PMS systems. A control test was carried out in the absence of PMS, wherein 100 mg L^{-1} of 50 mL of OG was mixed with 0.1 g L^{-1} of catalyst at its natural pH = 6.6, under regular stirring and at ambient temperature, whereas the catalytic process was then initiated in the solution by introducing 0.2 g L^{-1} (0.33 mM) of PMS. Hence, at regular specific times, a volume of 2 mL was withdrawn from the reaction medium, collected, then separated through 0.45 μm filter membranes, and finally analyzed. The catalyst efficacy was evaluated through the assessment of the contaminant removal amount, for various contaminants including MO, MB, and RhB, and by using a similar experimental protocol as for OG degradation. The mineralization efficiency of OG in the CoCN–$NaBH_4$/PMS system is typically measured using chemical oxygen demand (COD) by a colorimetric method based on Standard Methods for the Examination of Water and Wastewater. To detect the presence of reactive oxygen species (ROS) resulting *via* PMS activation, various quantities of radical scavengers, including methanol (MeOH), and *tert*-butyl-alcohol (TBA), were introduced into the catalyzed solution, in order to quench $SO_4^{\bullet-}$ and $HO^{\bullet}$, respectively. Furthermore, *p*-benzoquinone and L-histidine (L-his) were used as $O_2^{\bullet-}$ and $^1O_2$ scavengers. The accuracy of the results has been provided through running the experiments in duplicate or triplicate. The obtained data were averaged and plotted with error bars on the graphs. A UV-Vis spectrophotometer (6705 UV/Vis JENWAY) was used to determine the remaining concentration in the supernatant of different pollutants including OG, MO, MB and RhB. The measurements were conducted at specific wavelengths for each pollutant, namely, λ = 478 nm for OG, λ = 465 nm for MO, λ = 664 nm for MB, and λ = 554 nm for RhB. Moreover, for the purpose of detecting ROS involvement in the degradation process, we conducted *in situ* electron paramagnetic resonance (EPR) analyses. To achieve this, 50 μL of the reaction medium from each sample was transferred into a glass capillary sealed with Crit-O-seal TM. These capillaries were then positioned within an ESR-tube measuring an outer diameter of 5 mm. During the EPR experiments, *N-tert*-butyl-α-phenylnitrone (PBN) was employed as a spin-trapping agent to capture $HO^{\bullet}$ and $SO_4^{\bullet-}$, while 2,2,6,6 tetramethylpiperidine (TEMP) was chosen as a spin-trapping agent for $^1O_2$. Continuous-wave EPR spectra were captured at room temperature in an aerated medium using an EMX-plus X-band spectrometer from Bruker.

5. Results and discussion

5.1. Catalyst characterization

The chemical structure of the pure g-C_3N_4 matrix was confirmed through a series of analytical techniques, including TGA, XPS, and ^{13}C NMR spectroscopy.

5.1.1. TGA. Fig. 1 depicts the TGA of g-C_3N_4. As can be observed in Fig. 1, a distinct and net weight loss was revealed within the temperature range of 500 to 700 °C, which corresponds to the thermal decomposition of the g-C_3N_4 skeleton resulting in volatile gases containing C and N elements. These findings demonstrate the absence of inorganic impurities within the g-C_3N_4 structure.

5.1.2. XPS analysis. XPS survey spectra of the prepared g-C_3N_4 (Fig. 2a) reveal the presence of peaks located at 287.1, 398.1, and 531.1 eV, which are associated with the existence of C, N, and O elements, respectively. To gain a deep insight into the g-C_3N_4 surface chemical functions, a deconvolution of each peak was performed. Thus, the C 1s peak (Fig. 2b) exhibits the presence of three Gaussian distributions located at 284.6, 287.4, and 288.3 eV, which are indicative of (C–C) bonds, sp^2

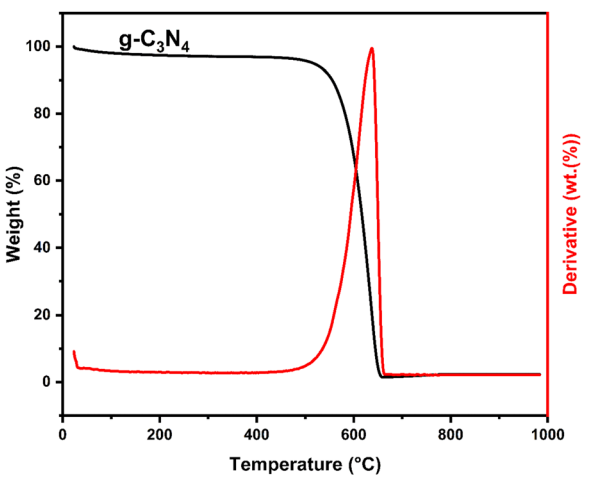

Fig. 1 TGA curve of g-C_3N_4.

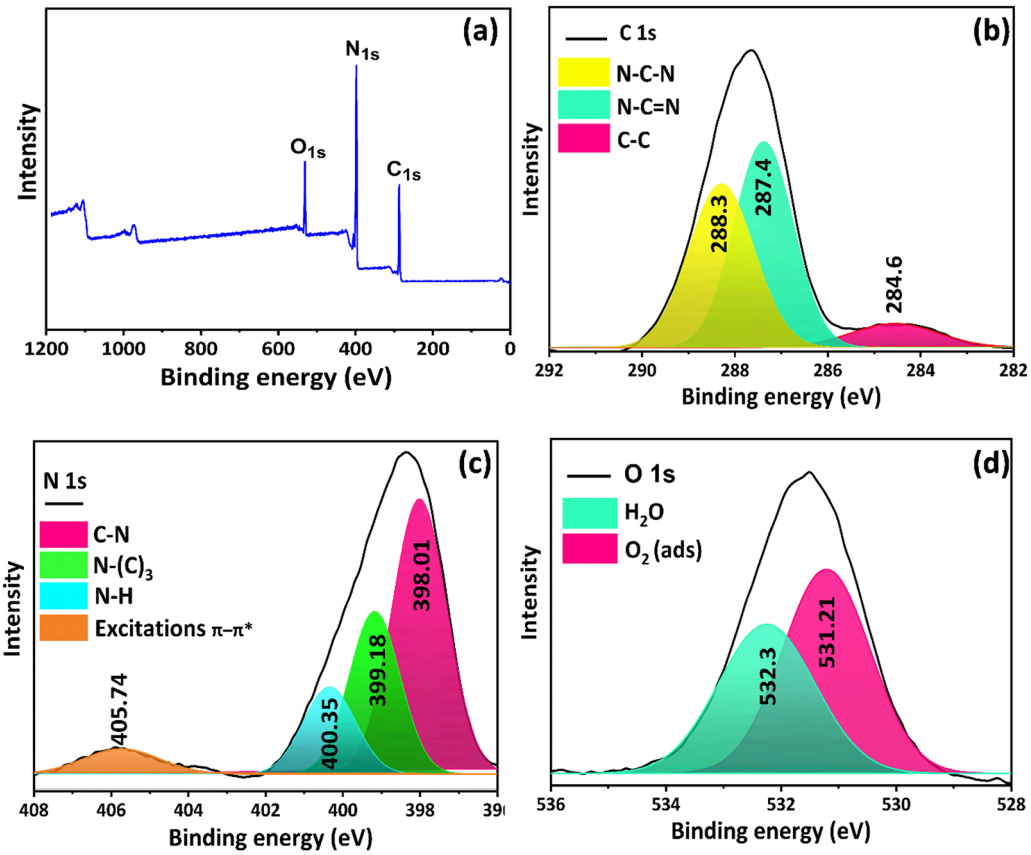

Fig. 2 (a) XPS survey spectrum, and high resolution XPS spectra of (b) C 1s, (c) N 1s, and (d) O 1s of g-C_3N_4.

hybridized carbon (N–C═N), and sp^2 hybridized carbon atoms bonded to N in an aromatic cycle (N–C–N), respectively.[44] The N 1s peak (Fig. 2c) revealed the presence of four peaks at 398.01, 399.18, 400.35, and 405.75 eV, which were attributed to (C–N), (N–$(C)_3$), (N–H), and π–π* excitations between stacking intercalators, respectively.[45] The O 1s peak (Fig. 3c) was deconvoluted into two peaks at 532.1 and 533.5 eV, corresponding to surface-adsorbed water and oxygen molecules, respectively.[46] These findings confirmed the expected g-C_3N_4 chemical structure.

5.1.3. ^{13}C NMR analyses. The ^{13}C NMR spectrum of g-C_3N_4 obtained using the CP/MAS method has been previously published elsewhere[43] by our co-workers. According to these results two unique and characteristic resonance groups were seen for the g-C_3N_4 sample. The first groups at 165.1 and 163.0 ppm were assigned to the carbon atoms (C1) linked to the –NH_2 groups, also known as (N_2)C(NH_2) groups. At 156 ppm, the second group correlated with the C atoms in the heptazine units and connected to N atoms (C($N)_3$). The aforementioned positions are consistent with the positions previously published for g-C_3N_4,[47–49] showing that the synthesized g-C_3N_4 was predominantly constituted of heptazine-based tectonic units.

5.1.4. XRD analysis. To investigate the changes in polymorph structure of g-C_3N_4 before and after chemical reduction with $NaBH_4$ or H_2, the XRD patterns were recorded on g-C_3N_4 and CoCN–$NaBH_4$ and CoCN–H_2 composites and they are presented in Fig. 3. Two characteristic peaks of the non-modified

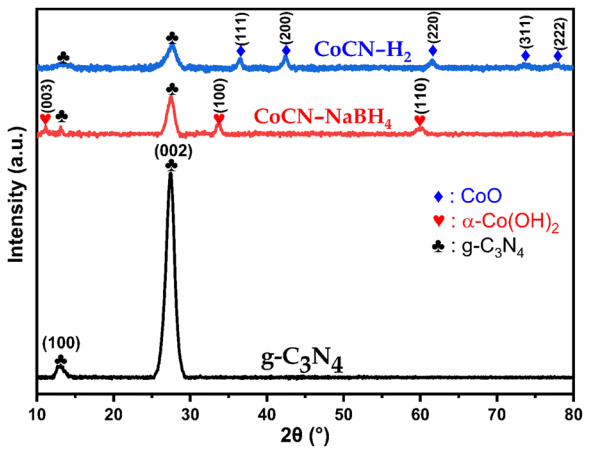

Fig. 3 XRD patterns of CoCN–H_2, CoCN–$NaBH_4$, and g-C_3N_4.

g-C_3N_4 were observed at 13.04° and 27.48° and they were identified as corresponding to the (100) and (002) planes, respectively, indicating the presence of tri-*s*-triazine units and the interlayer stacking of the conjugated tri-*s*-triazine nano sheet, respectively.[50] These two peaks characteristic of g-C_3N_4 were observed with a slight shift to a smaller angle in both cobalt-doped g-C_3N_4 catalysts (CoCN-*x*) as prepared by reduction reaction with $NaBH_4$ (peaks occurring at 2θ = 13.10° and 27.45°) and H_2 (peaks occurring at 2θ = 13.26° and

27.45°). This X-ray angle shift, accompanied by a decrease in the peak intensity, suggests the inhibition of urea polymeric condensation, which may be caused by the host–guest interaction occurring between the excessive cobalt species and the adjacent g-C_3N_4 layers.[51] The XRD pattern of CoCN–$NaBH_4$ displays additional diffraction peaks occurring at 2θ = 11.16°, 2θ = 33.65°, and 2θ = 60.08°, which correspond to the planes (003), (100), and (110) of α-$Co(OH)_2$ (JCPDS#46-0605)[52,53] Moreover, the XRD pattern of (CoCN–H_2), which was subjected to chemical reduction by H_2 under an argon (Ar) atmosphere, displays other diffraction peaks at 2θ = 36.54°, 2θ = 42.41°, 2θ = 61.57°, 2θ = 73.77°, and 2θ = 77.57°. These peaks are associated with (111), (200), (220), (311), and (222) planes of CoO (JCPDS#71-1178).[54]

5.1.5. FTIR analysis. The compositions and the structures of the g-C_3N_4, CoCN–H_2, and CoCN–$NaBH_4$ catalysts were confirmed by FTIR spectra (Fig. 4). Hence, the absorption peaks occurring at 2900–3400 cm^{-1} were associated with vibrations of free amino groups –NH that resulted from incomplete polymerization, as well as adsorbed hydroxyl species (–OH).[55–57] Meanwhile, the peaks at 1200–1650 cm^{-1} and the characteristic peak at 809 cm^{-1} correspond to the typical stretching modes of C–N heterocyclic rings and the vibration absorption of the triazine units, respectively.[43] The FTIR analyses of CoCN-*x* samples showed that the spectra of g-C_3N_4 remained unchanged after co-doping, except for a decrease in the peak intensity, as well as shifts in the peak positions. These findings suggest that the incorporation of Co species into the g-C_3N_4 structure took place, possibly along with a partial electron transfer from g-C_3N_4 to Co NPs,[58,59] which is in line with the XRD results.

5.1.6. SEM-EDS and TEM analyses. The morphologies and the microstructures of the three synthesized materials (g-C_3N_4, CoCN–$NaBH_4$ and CoCN–H_2) were characterized using both SEM and TEM.

Fig. 5 shows the morphologies of the g-C_3N_4, CoCN–$NaBH_4$, and CoCN–H_2 as obtained from the SEM analyses. The non-modified g-C_3N_4 sample (Fig. 5a) shows aggregated microstructures made up of a variety of irregular particles. However, upon the addition of cobalt to the g-C_3N_4 (Fig. 5b and c), the resulting agglomeration structures of CoCN–$NaBH_4$ and CoCN–H_2 were found to be identical to that of the non-modified g-C_3N_4. In addition to the SEM analyses, EDS mapping was conducted to identify the elemental composition and the relative abundance of the catalyst samples. The resulting data are presented in Fig. 5d–f, revealing the uniform dispersion of carbon, nitrogen, and oxygen throughout g-C_3N_4. However, additional cobalt species were observed in the CoCN-*x* composites, which corroborates the successful incorporation of cobalt into the g-C_3N_4 structure.

To get more insights into the catalysts' morphologies and microstructures, TEM analysis was performed for g-C_3N_4, CoCN–$NaBH_4$ and CoCN–H_2 materials, and the images of the three samples are shown in Fig. 6a–c, revealing a commonality in their structures as they all exhibit a nano-layer structure with a two-dimensional (2D) sheet-like morphology. The cobalt (black portion) was deposited in the g-C_3N_4 during the liquid phase reduction by $NaBH_4$ (Fig. 6b). On the other hand, chemical reduction with H_2 (Fig. 6c) resulted in well-defined dense and spherical cobalt particles, having a homogeneous size of around 9.51 nm, and distributed in the g-C_3N_4 nanosheets. However, as shown in Fig. 6c, cobalt particles appear agglomerated to some extent due to the g-C_3N_4 nanosheets stacked on top of each other.

5.1.7. BET–BJH analysis. Fig. 7 displays the N_2 adsorption–desorption isotherms and the BJH pore size distribution curves of g-C_3N_4, providing insights into its porous properties. Further, the observed hysteresis loop, conforming to the type IV isotherm with an H3-type hysteresis loop (Fig. 7a), clearly indicates the mesoporous nature of g-C_3N_4. The calculated specific surface area of g-C_3N_4 from the N_2 adsorption–desorption isotherm analysis gives a value of 62.44 m^2 g^{-1}. Furthermore, the pore volume and the average pore diameter of g-C_3N_4, obtained from the BJH pore size distribution (Fig. 7b), are 0.23 cm^3 g^{-1} and 44.07 nm, respectively.

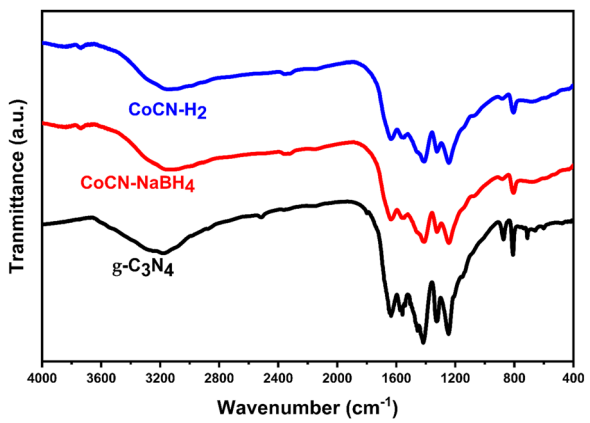

Fig. 4 FTIR spectra of CoCN–H_2, CoCN–$NaBH_4$, and g-C_3N_4.

6. Catalytic activity for the PMS activation

The novel synthesized catalysts' efficiency for the OG removal using PMS activation was examined, and the obtained results are graphically represented in Fig. 8. In the absence of PMS, the individual use of CoCN–H_2, CoCN–$NaBH_4$, and g-C_3N_4 catalysts results in the OG removal rates of less than 7%, 6%, and 6%, respectively (Fig. 8a). This observation supports the idea that the amount of the OG molecules physically adsorbed onto the catalyst surface is very low and it can be regarded as negligible. Moreover, the direct oxidation of OG without the presence of a catalyst using only PMS resulted in a limited 5% removal in a span of 6 minutes. This clearly highlights the challenge of oxidizing the OG dye solely with PMS without the activation provided by a catalyst. However, the CoCN–$NaBH_4$/PMS system achieved complete degradation of OG in a remarkably swift 2-minute timeframe, while the CoCN–H_2/PMS hybrid achieved the same result in just 6 minutes. The investigation into the

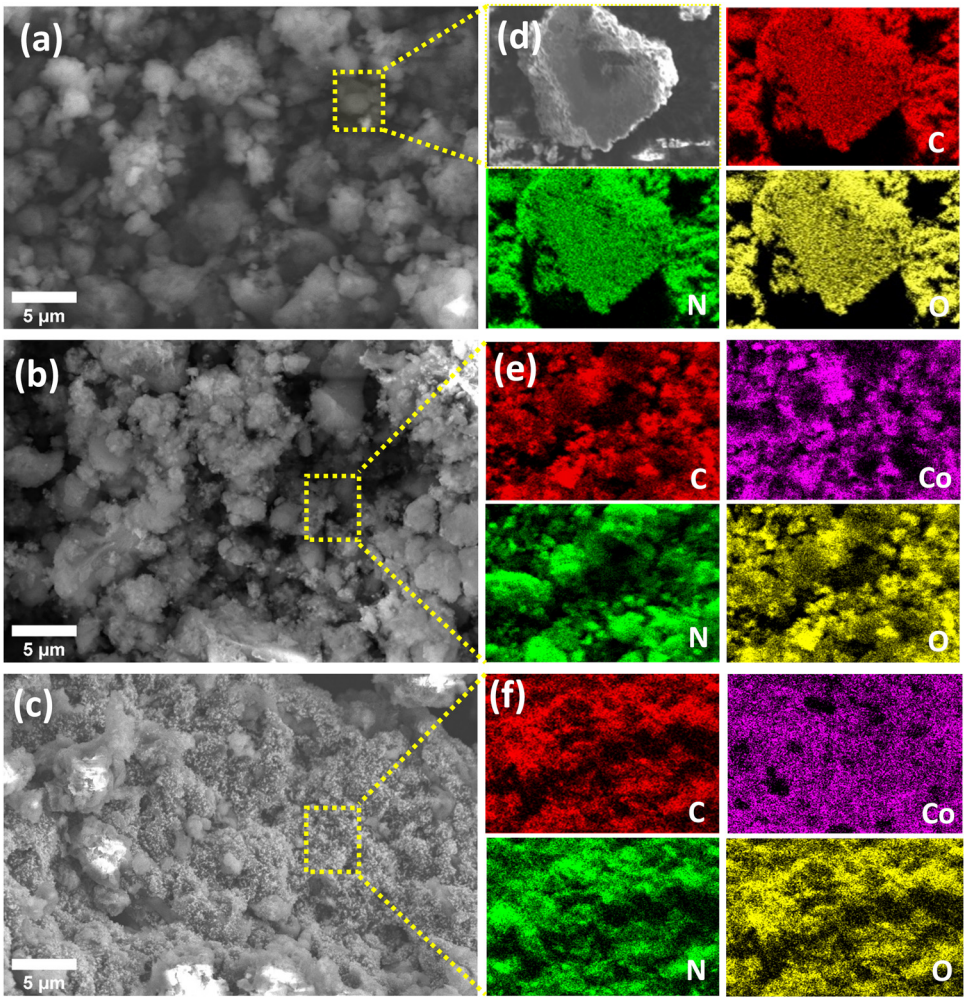

Fig. 5 SEM micrographs and EDS mapping of (a) and (d) g-C_3N_4, (b) and (e) CoCN–$NaBH_4$, and (c) and (f) CoCN–H_2.

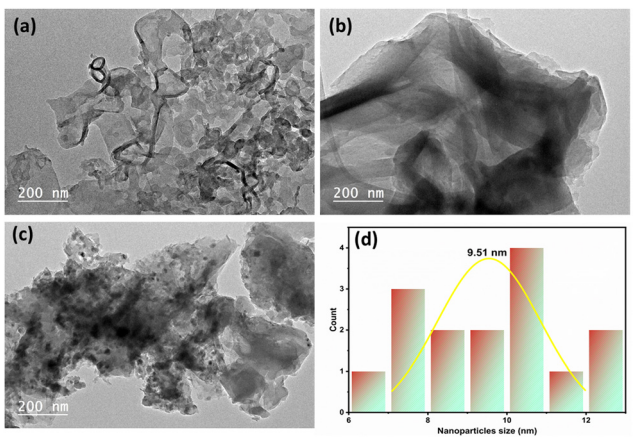

Fig. 6 TEM analysis of (a) g-C_3N_4, (b) CoCN–$NaBH_4$, and (c) CoCN–H_2. (d) NP size distribution histogram of CoCN–H_2.

efficacy of the CoCN-*x*/PMS system involved the use of COD analysis to gain insight into the mineralization outcomes after the degradation process. The COD analysis results are presented in Fig. 8c and d. Notably, the mineralization process exhibited a considerably slower rate compared to the discoloration of OG, owing to the increased challenge in degrading by-products relative to their original compounds. Specifically, approximately 76.2% and 86.9% COD removal were achieved after 30 min for CoCN–H_2/PMS and CoCN–$NaBH_4$/PMS, respectively. Furthermore, this efficiency remained nearly constant up to 90 min, indicative of a potential saturation limit. This phenomenon could be explained by the insufficient initial amount of PMS introduced.[60] The COD results collectively affirm the favorable mineralization observed in both CoCN-*x*/PMS systems, thereby implying an enhanced conversion efficiency of OG into H_2O and CO_2. These findings highlight the exceptional catalytic efficacy of the two catalysts in the process of activating PMS. Therefore, the introduction of cobalt into g-C_3N_4 yields a remarkable synergistic effect, enhancing the ROS generation through the catalysis of PMS. These ROS are found to be effective in decomposing the OG dye.[61,62]

The g-C_3N_4, owing to its exceptional degree of graphitization and uniform dispersion of Co NPs, has been found to significantly promote electron transfer throughout PMS and Co NPs.[63] This, in

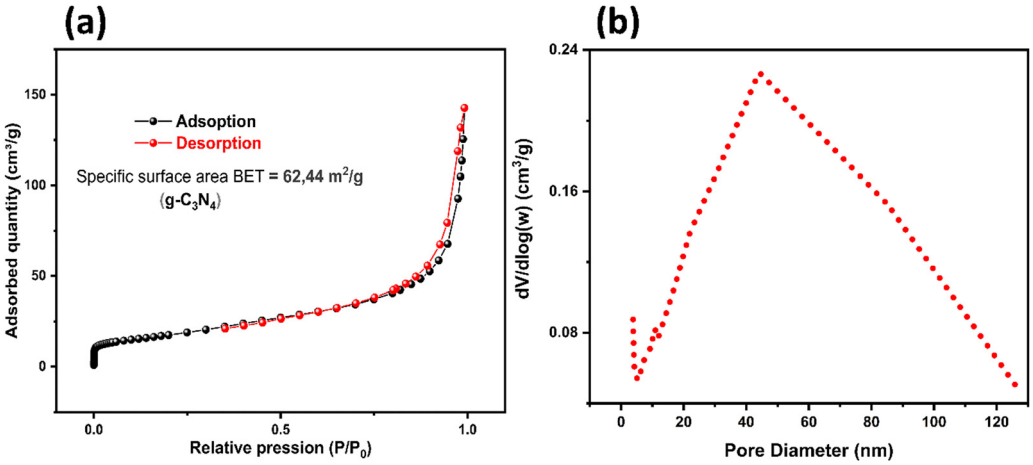

Fig. 7 BET isotherms (a) and pore-size distribution curve (b) of the g-C_3N_4 support.

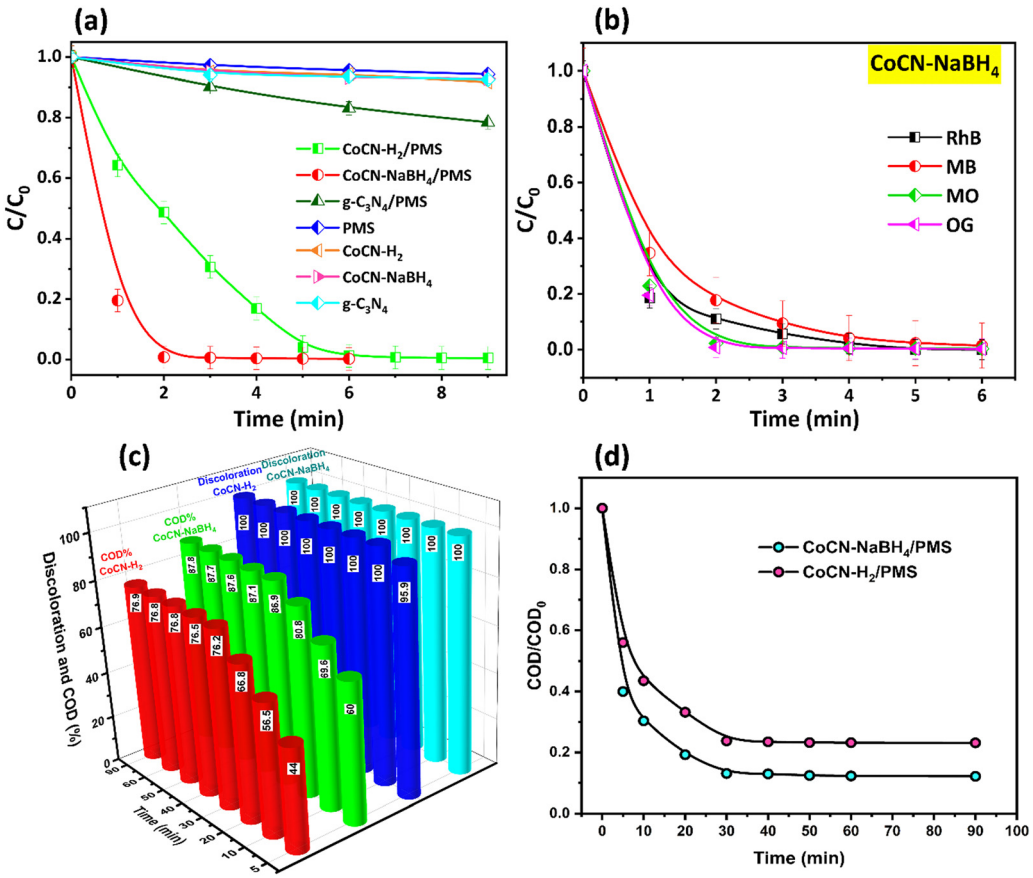

Fig. 8 (a) Removal rates of OG in various systems; (b) degradation of different pollutants using the CoCN–$NaBH_4$ catalyst; (c, d) COD removal of OG in the CoCN-*x* system.

turn, has facilitated the generation and conveyance of reactive radicals. Furthermore, the Co particle size on the g-C_3N_4 nanosheets was determined to be approximately 9.51 nm, as assessed by the TEM analyses, which seems to have a significant impact on the conductivity and the ROS production from the PMS activation.[64] These findings offer unambiguous proof that the g-C_3N_4, possessing a considerable functional group concentration, enabled the maintenance of a consistent Co nanoparticle size and allowed their homogeneous distribution within the g-C_3N_4, ultimately leading to a notable improvement in catalytic performance.

Several previous studies[65–67] have documented the remarkable effectiveness of hydroxylated metal species, particularly of

α-$Co(OH)_2$, as the primary catalyst for PMS activation, corroborating the findings of our own investigation. This heightened efficiency can be attributed to multiple factors, including its high surface area, abundant availability, rapid ion insertion/desertion kinetics, and distinctive redox properties. Furthermore, the considerable cost advantage associated with this catalyst has garnered considerable attention, offering an attractive alternative to thermal treatment synthesis methods typically required for other structures such as Co_3O_4 and CoO.[66,68] Thus, employing PMS as an oxidant, the catalytic activity of CoCN–$NaBH_4$ was assessed for the breakdown of various organic pollutants such as MO as an anionic dye and RhB and BM (cationic dyes). Fig. 8b shows that the majority of the pollutants degrade to zero within a maximum of 6 minutes. Hence, the comparison of CoCN-*x*/PMS systems with other studied state-of-the-art highly g-C_3N_4-supported cobalt oxide species catalysts for PMS activation towards removing different organic pollutants is shown in Table 1. It can be seen that the catalytic activity of both CoCN–$NaBH_4$ and CoCN–H_2 is excellent and much better in comparison to the other catalysts, indicating that the CoCN-*x*/PMS used in the current work is a performant system for removing organic pollutants from water bodies in a very short duration with no additional visible light irradiation required at room temperature. As a result, the CoCN–$NaBH_4$ catalyst investigated in the current work may facilitate the decomposition of PMS to produce active species suited for the oxidation of many kinds of organic contaminants.

7. Effect of the reaction parameters

To explore the impact of various experimental conditions on the OG degradation, such as the nature of water containing the pollutant, the catalyst, the PMS dosages and initial solution pH, the system CoCN–$NaBH_4$/PMS was selected since it was found to be more efficient and completely degrade the OG, in a shorter time, in comparison to the CoCN–H_2/PMS system. Thus, as can be seen in Fig. 9a, the rate of the OG degradation increased with increasing the catalyst dosage. A higher catalyst dosage (0.15 g L^{-1}) was found to completely degrade the OG in 1 minute, while a lower catalyst dosage (0.05 g L^{-1}) required more than 4 minutes. To summarize, the excellent catalytic activity of CoCN–$NaBH_4$ can be assigned to the formation of numerous active sites on its surface, which facilitate the electron transfer from the catalyst to the PMS, leading to an increase in the ROS production. Likewise, as depicted in Fig. 9b, the increase of the PMS concentration has a favourable influence on the reaction kinetics, where an increase from 0.16 to 0.41 mM of PMS results in more efficient electrostatic interactions, occurring between the electrophilic CoCN–$NaBH_4$

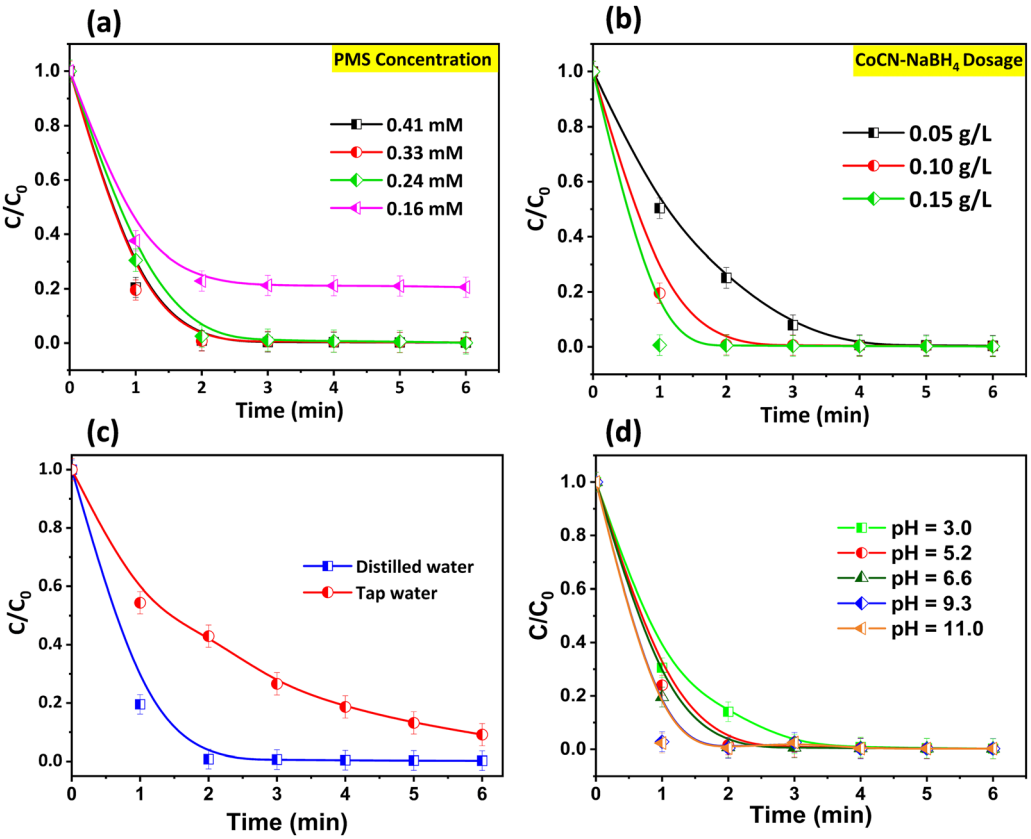

Fig. 9 Effects of (a) CoCN–$NaBH_4$ loading, (b) PMS dosage, (c) tap water, and (d) initial solution pH on the OG degradation using the CoCN–$NaBH_4$/PMS system.

surface sites and the HSO_5^- nucleophile, leading to the release of significant ROS amounts. The effect of tap water (TW) on the removal of OG by the CoCN–$NaBH_4$/PMS system was studied (Fig. 9c). The tap water matrix was taken from the University Ibn Zohr Agadir. The degradation efficiency of OG in distilled water (normal condition) was 100%, while the degradation efficiency in TW was 57% in 2 minutes. This difference in the OG degradation efficiency may be ascribed to the elevated conductivity and the existence of Cl^- ions in the tap water, which mitigate the ROS production. Nevertheless, it is noteworthy that the CoCN–$NaBH_4$/PMS system is suitable for the OG removal from real water samples. The role of initial pH in practical applications is crucial to the degradation of organic pollutants. To this end, various pH tests in a range of (3–11) were conducted on the CoCN–$NaBH_4$/PMS system, as depicted in Fig. 9d. The results demonstrate noteworthy OG decomposition efficiencies with the increase of pH value from 3 to 11. In particular, at an initial pH of 11, the degradation of OG reached nearly 100% within a remarkable timeframe of 1 min, contrasting with the scenario at pH 3, where complete OG degradation required 3 min. This observed discrepancy can be attributed to several underlying factors. Under acidic conditions, H^+ ions may effectively scavenge radical species such as $SO_4^{\bullet-}$ and $OH^\bullet$ (eqn (1) and (2)).[79] Additionally, the higher concentration of singlet oxygen ($^1O_2$) could be generated due to the transformation of PMS to SO_5^{2-} (as represented by eqn (3) and (4)).[29] Finaly, raising the pH additionally promoted the production of hydroxyl radicals on the surface of the CoCN–$NaBH_4$ catalyst. $OH^\bullet$ serve as active sites for electron transfer, thereby bolstering the catalyst's effectiveness. Overall, the CoCN–$NaBH_4$/PMS system exhibited high degradation reaction of OG over a wide pH range of 3.0–11.0.

$$OH^\bullet + H^+ + e^- \rightarrow H_2O \quad (1)$$

$$SO_4^{\bullet-} + H^+ + e^- \rightarrow HSO_4^- \quad (2)$$

$$HSO_5^- \rightarrow SO_5^{2-} + H^+ \quad (3)$$

$$HSO_5^- + SO_5^{2-} \rightarrow SO_4^{2-} + HSO_4^{2-} + {}^1O_2 \quad (4)$$

8. Reactive oxygen species (ROS) identification and PMS activation mechanism

In order to identify the main ROS generated in the CoCN–H_2/PMS and CoCN–$NaBH_4$/PMS systems and responsible for the orange G degradation, radical scavenging experiments were conducted, and the results are presented in Fig. 10. Based on

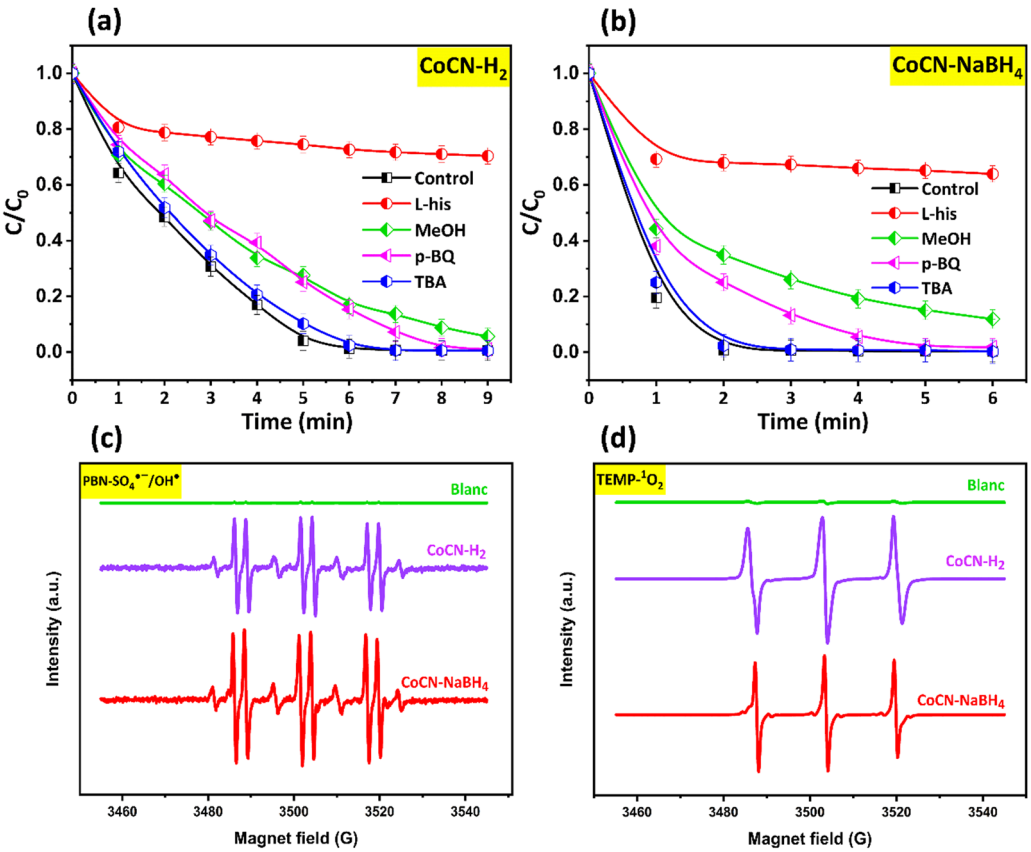

Fig. 10 Scavenger effect experiments on OG removal in (a) the CoCN–H_2/PMS system, and (b) CoCN–$NaBH_4$/PMS system, and EPR signals of different active free radicals (c) PBN-$SO_4^{\bullet-}$/$OH^\bullet$ and (d) TEMPO-$^1O_2$.

the literature, the PMS activation typically may generate either $SO_4^{\bullet -}$, $HO^{\bullet}$ and $O_2^{\bullet -}$ radical species, or non-radical singlet oxygen ($^1O_2$).[80] Methanol (MeOH) is used as a scavenger for radicals $HO^{\bullet}$ (9.7×10^8 M^{-1} s^{-1}) and $SO_4^{\bullet -}$ (2.5×10^7 M^{-1} s^{-1}).[81,82] Compared to $SO_4^{\bullet -}$ (4.0–9.1 $\times$ 10^5 M^{-1} s^{-1}), *tert*-butanol (TBA) is more efficient for $HO^{\bullet}$ (3.8–7.6 $\times$ 10^8 M^{-1} s^{-1}).[81,82] Furthermore, *p*-benzoquinone (*p*-BQ) is used to check the presence of $O_2^{\bullet -}$ (k = 0.9–1 10^9 M^{-1} s^{-1}),[83] and L-histidine (L-His) is used as a sensor to check the presence of non-radical species $^1O_2$ (k = 3,2 $\times$ 10^7 M^{-1} s^{-1}).[84] Fig. 10a and b shows that, among all scavengers investigated, 300 mM TBA was found to have little impact on the OG degradation rate in the catalytic system. Thus, according to the overall OG degradation results obtained in the presence of TBA scavenger, it can be argued that the contribution of $HO^{\bullet}$ towards OG removal was negligible. However, as shown in Fig. 10a and b, the addition of 300 mM MeOH was found to decrease the OG degradation rates, in the CoCN–$NaBH_4$/PMS and in the CoCN–H_2/PMS systems. Specifically, the degradation rates decreased to 65% within 2 minutes for CoCN–$NaBH_4$/PMS and to 83% within 7 minutes for CoCN–H_2/PMS, in comparison to the initial rate of 100% obtained in the absence of MeOH. These results indicate that the OG degradation is partially facilitated by $SO_4^{\bullet -}$ radicals to some extent in the CoCN-*x*/PMS system. However, the contribution of $SO_4^{\bullet -}$ radicals in the reaction system was found to be restricted, suggesting the participation of additional reaction pathways. Moreover, the introduction of L-histidine at low concentration (2 mM) into the reaction system resulted in a noteworthy inhibition of OG degradation. In contrast, the introduction of an identical *p*-BQ concentration (2 mM) in the reaction medium did not lead to a significant OG degradation, indicating a minor involvement of $O_2^{\bullet -}$ in the degradation reaction, and increasing the likelihood of occurrence of a non-radical pathway ($^1O_2$). Therefore, it can be said that the cobalt doping process in g-C_3N_4 is a highly effective strategy for enhancing the active site abundance on the material surface. This, in turn, facilitates the degradation process, mainly through a non-radical pathway, primarily induced by the generation of $^1O_2$. Our results are in accordance with previously reported works using various systems such as Co-NC-PS,[45] Co_3O_4/g-C_3N_4,[76] CoS/g-C_3N_4,[85] Co-N/C,[86] and Co-O@CN.[87] As a result, it can be concluded that cobalt doping plays a pivotal role in augmenting the presence of active sites and promoting the efficient degradation of organic pollutants. The verification and confirmation of ROS involvement in the degradation reaction of OG were established through EPR analysis, utilizing PBN as a spin-trapping agent for $SO_4^{\bullet -}$ and $HO^{\bullet}$, and TEMP as a spin-trapping agent for $^1O_2$ across diverse catalytic reactions.[88] As depicted in Fig. 10c and d, a linear trace was observed in the presence of either PBN or TEMP agent when PMS operated alone in various catalytic processes, signifying the absence of radical generation. Conversely, distinctive peaks emerged in the EPR spectra when PMS activation occurred in the presence of different catalysts. Hence, the EPR spectra (Fig. 10c) vividly exhibit characteristic signals for PBN- $SO_4^{\bullet -}$ and PBN-$HO^{\bullet}$, implying the creation of $SO_4^{\bullet -}$ and $HO^{\bullet}$ radicals in diverse CoCN-*x*/PMS systems. Moreover, the amplitudes of the PBN- $SO_4^{\bullet -}$ and PBN- $HO^{\bullet}$ signals were notably higher in the CoCN–$NaBH_4$/PMS system compared to the PBN-X signals in the CoCN–H_2/PMS systems, indicating a substantial generation of radicals in the CoCN–$NaBH_4$/PMS system. Importantly, a distinct robust triplet signal consistently appeared when TEMP was employed as the spin agent for both CoCN-*x* systems (Fig. 10d), affirming the production of $^1O_2$ in the various oxidation systems under scrutiny.

The degradation mechanism is still debatable and requires further elucidation in the future. Further, the activation of PMS in heterogeneous systems has received considerable attention owing to its potential for advanced oxidation processes. A particular system of interest entails the occurrence of electron transfer reactions occurring between cobalt ions that are doped onto g-C_3N_4 and PMS. The CoCN-*x*/PMS system, investigated in the present study, bears a resemblance to the conventional Fenton reaction. The aim of the work is to highlight the mechanism underlying the PMS activation by CoCN-*x*, as described in Fig. 11. It is worth mentioning that the Co/PMS catalyst system has been demonstrated to effectively facilitate oxidative processes *via* both radical and non-radical mechanisms in the decomposition of organic contaminants.[89] It can be inferred that the underlying mechanism of PMS-derived oxidation processes is intricately related to not only the type of catalyst employed (with particular emphasis on the interactions between active metal centers and diverse supports) but also the adsorptive characteristics of the organic compounds.[90] In addition, the Co atoms in CoCN-*x* exist mainly as Co(II) and Co(III), and according to the redox potential of the HSO_5^-/SO_5^- (0.95–1.24 V) and Co(II)/Co(III) (1.92 V),[79,91] they facilitate the generation of $SO_4^{\bullet -}$ and $HO^{\bullet}$. During the OG degradation, the PMS molecules adsorb firstly onto the CoCN-*x* catalyst surface. Following that, under the catalytic effect of Co(II), the PMS O–O bond undergoes dissociation, leading to the generation of $SO_4^{\bullet -}$ and $OH^{\bullet}$ (eqn (5) and (6)). In another step, Co(II) also promotes the generation of Co(III), which could oxidize PMS for further $OH^{\bullet}$ and $SO_5^{\bullet -}$ generation (eqn (7)).[92] This catalytic electron transfer mechanism ensures a continuous generation of Co^{2+} and Co^{3+}, thereby facilitating the overall catalytic reaction.[90] Trapping experiments by using various scavengers have revealed that the $^1O_2$, generated through the non-radical pathway, is the dominant oxidant species in the CoCN-*x*/PMS system. Likewise, the formed $SO_5^{\bullet -}$ may engage in various reactions through multiple possible pathways with H_2O and HSO_5^-, or even react in pairs, ultimately leading to the production of $^1O_2$[85,93,94] (eqn (8)–(10)). Additional pathways for $^1O_2$ production have been proposed, as elucidated by (eqn (11)–(14)),[88] wherein these pathways involve the contribution of $O_2^{\bullet -}$, whose generation has been corroborated by quenching experiments conducted during OG degradation. The various oxidant species ($^1O_2$, $O_2^{\bullet -}$, $SO_4^{\bullet -}$, and $HO^{\bullet}$) produced by the CoCN-*x*/PMS system directly degraded pollutants (eqn (15)).

$$HSO_5^- + Co^{2+} \rightarrow SO_4^{\bullet -} + OH^- + Co^{3+} \quad (5)$$

$$HSO_5^- + Co^{2+} \rightarrow OH^{\bullet} + SO_4^{2-} + Co^{3+} \quad (6)$$

$$HSO_5^- + Co^{3+} \rightarrow SO_5^{\bullet -} + Co^{2+} + H^+ \quad (7)$$

$$2SO_5^{\bullet -} + H_2O \rightarrow 2H^+ + 2SO_4^{2-} + 1.5\ ^1O_2 \quad (8)$$

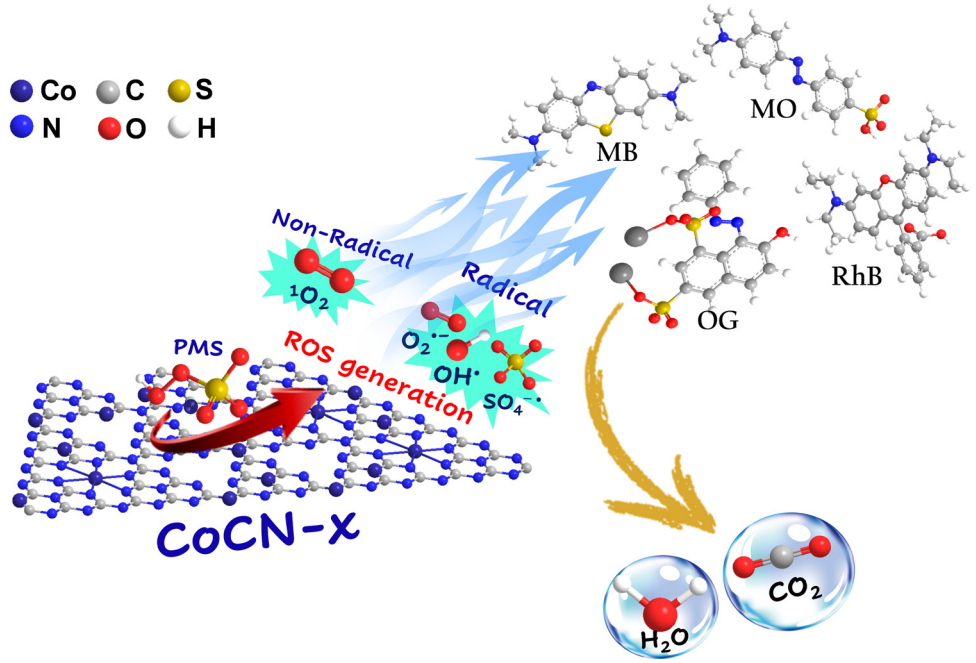

Fig. 11 Possible synergistic degradation mechanism of OG by the CoCN-*x*/PMS system.

$$SO_5^{\bullet-} + HSO_5^- \rightarrow HSO_4^- + SO_4^{2-} + {}^1O_2 \quad (9)$$

$$2SO_5^{\bullet-} \rightarrow S_2O_8^{2-} + {}^1O_2 \quad (10)$$

$$HSO_5^- + H_2O \rightarrow HSO_4^- + H_2O_2 \quad (11)$$

$$Co^{3+} + H_2O_2 \rightarrow HO_2^{\bullet} + H^+ + Co^{2+} \quad (12)$$

$$HO_2^{\bullet} \rightarrow O_2^{\bullet-} + H^+ \quad (13)$$

$$O_2^{\bullet-} + OH^{\bullet} \rightarrow OH^- + {}^1O_2 \quad (14)$$

$$({}^1O_2 + SO_4^{\bullet-} + O_2^{\bullet-} + OH^{\bullet})/\text{organic pollutants} \rightarrow \text{Decomposed products} \quad (15)$$

9. Conclusion

In summary, we designed cobalt-doped graphitic carbon nitride catalysts *via* two reduction methods using $NaBH_4$ (liquid phase) and H_2 (gas phase). At first, the g-C_3N_4 structure was confirmed by using several characterization methods including XPS, ^{13}C NMR and TGA. Further, the crystalline phases and the structural properties of cobalt doped g-C_3N_4 (CoCN-*x*) were assessed with XRD, FTIR, SEM-EDS, and TEM analyses. The results obtained confirmed that we have successfully prepared efficient catalysts, and indicated that the incorporated Co species in the g-C_3N_4 nanosheets for the two CoCN–$NaBH_4$ and CoCN–H_2 catalysts exist in two forms α-$Co(OH)_2$ and CoO, respectively. The cobalt-doped g-C_3N_4 (CoCN-*x*) were found to be excellent PMS activators. Further, they could be considered as green catalysts since their application reduces secondary pollution owing to their magnetic properties, which facilitate their separation from aqueous media. In addition, the present work has led to identify and to assess the cobalt doped carbon in CoCN-*x* active sites for activating the PMS, in heterogeneous catalysis *via* the electron transfer mechanism, towards various dye degradation. The overall data showed a significant improvement in catalytic performance, as evidenced by the production of a higher percentage of ROS by using cobalt doped g-C_3N_4 (CoCN-*x*) in comparison to the non-doped g-C_3N_4, resulting from the synergistic effect occurring between the cobalt oxide (α-$Co(OH)_2$ or CoO) and the g-C_3N_4.

The catalytic OG degradation data have shown that radical and non-radical pathways could coexist throughout different CoCN-*x*/PMS systems, but singlet oxygen $^1O_2$, which was generated through the non-radical mechanism, dominates, as evidenced by the scavenger tests and EPR analysis that we have carried out. Thus, the explanations for the predominance of the non-radical pathway and the dynamic interaction of CoCN–$NaBH_4$ and CoCN–H_2 catalysts with various types of pollutants must be studied more deeply.

Conflicts of interest

The authors declare that they have no known competing financial interests or personal relationships that could have appeared to influence the work reported in this paper.

Acknowledgements

The present research is the consequence of a collaborative endeavour that includes scientific researchers from the Faculté des Sciences d'Agadir, Université Ibn Zohr, Agadir-Morocco, and Institut de Sciences des Matériaux De Mulhouse (IS2M-UMR 7361CNRS), Université de Haute Alsace (UHA), Mulhouse-France. We thank

VIDAL Loïc (IS2M-Mulhouse-France), VAULOT Cyril (IS2M-Mulhouse-France), and FIOUX Philippe (IS2M-Mulhouse-France), for the Transmission electron microscopy (TEM) analyses, the BET–BJH analyses, and the X-Ray photoelectron spectrometry analyses, respectively.

References

1 B. E. Channab, M. El Ouardi and S. E. Marrane, *et al.*, Alginate@$ZnCO_2O_4$ for efficient peroxymonosulfate activation towards effective rhodamine B degradation: optimization using response surface methodology, *RSC Adv.*, 2023, **13**(29), 20150–20163, DOI: 10.1039/D3RA02865H.

2 A. Ahdour, A. Taoufyq, L. Aneflous, B. Bakiz and A. Benlhachemi, Electrochemical and photoelectrochemical degradation of Rhodamine B using a novel BHP@ZnO photoelectrode: Synthesis, characterization, and statistical study, *Colloids Surf., A*, 2023, **678**, 132427, DOI: 10.1016/j.colsurfa.2023.132427.

3 S. Farsad, A. Amjlef and A. Chaoui, *et al.*, Harnessing a carbon-based material from food waste digestate for dye adsorption: the role of hydrogel beads in enhancing the material stability and regenerative capacity, *Mater Adv.*, 2023, **4**(24), 6599–6611, DOI: 10.1039/D3MA00505D.

4 A. Imgharn, L. Anchoum and A. Hsini, *et al.*, Effectiveness of a novel polyaniline@Fe-ZSM-5 hybrid composite for Orange G dye removal from aqueous media: Experimental study and advanced statistical physics insights, *Chemosphere*, 2022, **295**, 133786, DOI: 10.1016/j.chemosphere.2022.133786.

5 Y. Ettahiri, L. Bouna and J. V. Hanna, *et al.*, Pyrophyllite clay-derived porous geopolymers for removal of methylene blue from aqueous solutions, *Mater. Chem. Phys.*, 2023, **296**, 127281, DOI: 10.1016/j.matchemphys.2022.127281.

6 A. Imgharn, H. Ighnih and A. Hsini, *et al.*, Synthesis and characterization of polyaniline-based biocomposites and their application for effective removal of Orange G dye using adsorption in dynamic regime, *Chem. Phys. Lett.*, 2021, **778**, 138811, DOI: 10.1016/j.cplett.2021.138811.

7 B. Akhsassi, A. Bouddouch and Y. Naciri, *et al.*, Enhanced photocatalytic activity of $Zn_3(PO_4)_2$/ZnO composite semiconductor prepared by different methods, *Chem. Phys. Lett.*, 2021, **783**, 139046, DOI: 10.1016/j.cplett.2021.139046.

8 A. Amjlef, S. Khrach, A. Ait El Fakir, S. Farsad, S. Et-Taleb and N. El Alem, Adsorptive properties investigation of natural sand as adsorbent for methylene blue removal from contaminated water, *Nanotechnol. Environ. Eng.*, 2021, **6**(2), 26, DOI: 10.1007/s41204-021-00119-y.

9 N. Nouj, N. Hafid and N. El Alem, *et al.*, Valorization of β-Chitin Extraction Byproduct from Cuttlefish Bone and Its Application in Food Wastewater Treatment, *Materials*, 2022, **15**(8), 2803, DOI: 10.3390/ma15082803.

10 A. Amjlef, S. Farsad and A. Ait El Fakir, *et al.*, Polyaniline-encapsulated quartz sand as an adsorbent composite for Orange G dye removal from aqueous solution: Experimental and computational study, *Ceram Int.*, 2023, **49**(9), 14120–14134, DOI: 10.1016/j.ceramint.2022.12.293.

11 A. Amjlef, S. Farsad and A. Chaoui, *et al.*, Effective adsorption of Orange G dye using chitosan cross-linked by glutaraldehyde and reinforced with quartz sand, *Int. J. Biol. Macromol.*, 2023, **239**, 124373, DOI: 10.1016/j.ijbiomac.2023.124373.

12 N. Iberache, F. E. Titchou and M. Errami, *et al.*, Removal of the Insecticide Imidacloprid from Water in Commercial Formulation using Electro-Fenton and Photo-Electro-Fenton: Optimization of COD Removal through Response Surface Methodology RSM-CCD, *Chem. Eng. Process.*, 2024, **196**, 109633, DOI: 10.1016/j.cep.2023.109633.

13 M. E. Housse, A. Hadfi and I. Karmal, *et al.*, Toxicity Profile, Phytochemical Composition, and Anti-scaling Properties of the Aqueous Extract of Ocimum basilicum L. Leaves as Novel Green and Cost-Effective Inhibitor: Experimental, MC/SAA and DFT Approach, *Waste Biomass Valorization*, 2023, **14**(11), 3553–3573, DOI: 10.1007/s12649-023-02066-y.

14 S. Farsad, Z. Anfar, A. Ait El Fakir, A. Amjlef, N. El Alem and I. Ionel, Methane recovery from the leachate of municipal solid waste landfill by using anaerobic digestion, Case Study, In European Biomass Conference and Exhibition Proceedings.; 2022, pp. 223–227.

15 S. Farsad, A. Ben Hamou and A. Chaoui, *et al.*, Maximizing bio-methane potential from municipal landfill leachate through ultrasonic pretreatment, *Heliyon*, 2023, **9**(11), e21347, DOI: 10.1016/j.heliyon.2023.e21347.

16 M. El Ouardi, O. Ait Layachi and E. Amaterz, *et al.*, Photoelectrochemical degradation of rhodamine B using electrodeposited $Mn_3(PO_4)_{2.3}H_2O$ thin films, *J. Photochem. Photobiol., A*, 2023, **444**, 115011, DOI: 10.1016/j.jphotochem.2023.115011.

17 B. E. Channab, M. El Ouardi and O. Ait Layachi, *et al.*, Recent trends on MIL-Fe metal–organic frameworks: synthesis approaches, structural insights, and applications in organic pollutant adsorption and photocatalytic degradation, *Environ. Sci.: Nano*, 2023, **10**(11), 2957–2988, DOI: 10.1039/D3EN00332A.

18 A. Elaouni, M. El Ouardi, A. BaQais, M. Arab, M. Saadi and H. Ait Ahsaine, Bismuth tungstate Bi 2 WO 6: a review on structural, photophysical and photocatalytic properties, *RSC Adv.*, 2023, **13**(26), 17476–17494, DOI: 10.1039/D3RA01987J.

19 D. Liu, Z. Su, B. Han, K. Xia, C. Zhou and Q. Gao, Cobalt–aluminum oxide clusters-embedded γ-Al2O3 nanosheets for peroxymonosulfate activation: Interfacial pH-buffering property to eliminate cobalt leaching and boost the catalytic activity, *Appl. Catal., B*, 2023, **330**, 122555, DOI: 10.1016/j.apcatb.2023.122555.

20 A. Amjlef, S. Farsad and A. Ait El Fakir, *et al.*, Polyaniline-encapsulated quartz sand as an adsorbent composite for Orange G dye removal from aqueous solution: Experimental and computational study, *Ceram. Int.*, 2023, **49**(9), 14120–14134, DOI: 10.1016/j.ceramint.2022.12.293.

21 A. Ait El Fakir, Z. Anfar and A. Amedlous, *et al.*, Engineering of new hydrogel beads based conducting polymers: Metal-

free catalysis for highly organic pollutants degradation, *Appl. Catal., B*, 2021, **286**, 119948, DOI: 10.1016/j.apcatb.2021.119948.

22 A. Ahdour, E. Amaterz and A. Taoufyq, *et al.*, Enhancing electrochemical and photoelectrochemical degradation of organic dyes under visible irradiation with a novel Cu_2O/$BaHPO_4$-based photoelectrode, *J. Alloys Compd.*, 2023, **960**, 170822, DOI: 10.1016/j.jallcom.2023.170822.

23 S. Lotfi, M. El Ouardi and H. Ait Ahsaine, *et al.*, Low-temperature synthesis, characterization and photocatalytic properties of lanthanum vanadate $LaVO_4$, *Heliyon*, 2023, **9**(6), e17255, DOI: 10.1016/j.heliyon.2023.e17255.

24 B. El Allaoui, H. Benzeid, N. Zari, A. el K. Qaiss and R. Bouhfid, Functional cellulose-based beads for drug delivery: Preparation, functionalization, and applications, *J. Drug Delivery Sci. Technol.*, 2023, **88**, 104899, DOI: 10.1016/j.jddst.2023.104899.

25 Z. Anfar, A. A. El Fakir and M. Zbair, *et al.*, New functionalization approach synthesis of Sulfur doped, Nitrogen doped and Co-doped porous carbon: Superior metal-free Carbocatalyst for the catalytic oxidation of aqueous organics pollutants, *Chem. Eng. J.*, 2021, **405**, 126660, DOI: 10.1016/j.cej.2020.126660.

26 A. Ait El Fakir, Z. Anfar and A. Amedlous, *et al.*, Synergistic effect for efficient catalytic persulfate activation in conducting polymers-hematite sand composites: Enhancement of chemical stability, *Appl. Catal., A*, 2021, **623**, 118246, DOI: 10.1016/j.apcata.2021.118246.

27 X. Duan, H. Sun and S. Wang, Metal-Free Carbocatalysis in Advanced Oxidation Reactions, *Acc. Chem. Res.*, 2018, **51**(3), 678–687, DOI: 10.1021/acs.accounts.7b00535.

28 M. Li, Z. Li and X. Yu, *et al.*, FeN4-doped carbon nanotubes derived from metal organic frameworks for effective degradation of organic dyes by peroxymonosulfate: Impacts of FeN4 spin states, *Chem. Eng. J.*, 2022, **431**, 133339, DOI: 10.1016/j.cej.2021.133339.

29 S. Wang and Y. Zhang, Zero valent iron-electro-Fenton-peroxymonosulfate (ZVI-E-Fenton-PMS) process for industrial wastewater treatment, *RSC Adv.*, 2023, **13**(22), 15063–15076, DOI: 10.1039/D2RA06653J.

30 M. Du, Q. Yi and J. Ji, *et al.*, Sustainable activation of peroxymonosulfate by the Mo(IV) in MoS2 for the remediation of aromatic organic pollutants, *Chin. Chem. Lett.*, 2020, **31**(10), 2803–2808, DOI: 10.1016/j.cclet.2020.08.002.

31 H. Li, Z. Zhao, J. Qian and B. Pan, Are Free Radicals the Primary Reactive Species in Co(II)-Mediated Activation of Peroxymonosulfate? New Evidence for the Role of the Co(II)–Peroxymonosulfate Complex, *Environ. Sci. Technol.*, 2021, **55**(9), 6397–6406, DOI: 10.1021/acs.est.1c02015.

32 X. Zhou, Q. Zhao, J. Wang, Z. Chen and Z. Chen, Nonradical oxidation processes in PMS-based heterogeneous catalytic system: Generation, identification, oxidation characteristics, challenges response and application prospects, *Chem. Eng. J.*, 2021, **410**, 128312, DOI: 10.1016/j.cej.2020.128312.

33 A. Y. Zhang, Y. Y. He, Y. P. Chen, J. W. Feng, N. H. Huang and F. Lian, Degradation of organic pollutants by Co_3O_4-mediated peroxymonosulfate oxidation: Roles of high-energy {0 0 1}-exposed TiO_2 support, *Chem. Eng. J.*, 2018, **334**, 1430–1439, DOI: 10.1016/j.cej.2017.11.078.

34 K. Y. A. Lin and B. J. Chen, Magnetic carbon-supported cobalt derived from a Prussian blue analogue as a heterogeneous catalyst to activate peroxymonosulfate for efficient degradation of caffeine in water, *J. Colloid Interface Sci.*, 2017, **486**, 255–264, DOI: 10.1016/j.jcis.2016.09.073.

35 K. Y. A. Lin, H. A. Chang and R. C. Chen, MOF-derived magnetic carbonaceous nanocomposite as a heterogeneous catalyst to activate oxone for decolorization of Rhodamine B in water, *Chemosphere*, 2015, **130**, 66–72, DOI: 10.1016/j.chemosphere.2015.03.025.

36 W. D. Oh, Z. Dong, Z. T. Hu and T. T. Lim, A novel quasi-cubic $CuFe_2O_4$–Fe_2O_3 catalyst prepared at low temperature for enhanced oxidation of bisphenol A via peroxymonosulfate activation, *J. Mater. Chem. A*, 2015, **3**(44), 22208–22217, DOI: 10.1039/C5TA06563A.

37 G. P. Anipsitakis and D. D. Dionysiou, Radical Generation by the Interaction of Transition Metals with Common Oxidants, *Environ. Sci. Technol.*, 2004, **38**(13), 3705–3712, DOI: 10.1021/es035121o.

38 W. Zhang, S. Zhang, C. Meng and Z. Zhang, Nanoconfined catalytic membranes assembled by cobalt-functionalized graphitic carbon nitride nanosheets for rapid degradation of pollutants, *Appl. Catal., B*, 2023, **322**, 122098, DOI: 10.1016/j.apcatb.2022.122098.

39 X. Duan, H. Sun, Y. Wang, J. Kang and S. Wang, N-Doping-Induced Nonradical Reaction on Single-Walled Carbon Nanotubes for Catalytic Phenol Oxidation, *ACS Catal.*, 2015, **5**(2), 553–559, DOI: 10.1021/cs5017613.

40 H. Zhang, L. Lyu, Q. Fang, C. Hu, S. Zhan and T. Li, Cation−π structure inducing efficient peroxymonosulfate activation for pollutant degradation over atomically dispersed cobalt bonding graphene-like nanospheres, *Appl. Catal., B*, 2021, **286**, 119912, DOI: 10.1016/j.apcatb.2021.119912.

41 M. Majdoub, Z. Anfar and A. Amedlous, Emerging Chemical Functionalization of g-C_3N_4: Covalent/Noncovalent Modifications and Applications, *ACS Nano*, 2020, **14**(10), 12390–12469, DOI: 10.1021/acsnano.0c06116.

42 A. Amedlous, M. Majdoub, E. Amaterz, Z. Anfar and A. Benlhachemi, Synergistic effect of g-C_3N_4 nanosheets/Ag_3PO_4 microcubes as efficient n-p-type heterostructure based photoanode for photoelectrocatalytic dye degradation, *J. Photochem. Photobiol., A*, 2021, **409**, 113127, DOI: 10.1016/j.jphotochem.2020.113127.

43 A. Amedlous, M. Majdoub, Z. Anfar and E. Amaterz, Self-Supporting g-C_3N_4 Nanosheets/Ag Nanoparticles Embedded onto Polyester Fabric as ''Dip-Catalyst'' for Synergic 4-Nitrophenol Hydrogenation, *Catalysts*, 2021, **11**(12), 1533, DOI: 10.3390/catal11121533.

44 M. Majdoub, A. Amedlous, Z. Anfar and A. Jada, Engineering of H-Bonding Interactions in PVA/g-C_3N_4 Hybrids for Enhanced Structural, Thermal, and Mechanical Properties: Toward Water-Responsive Shape Memory Nanocomposites,

Adv. Mater. Interfaces, 2022, **9**(14), 2200170, DOI: **10.1002/admi.202200170**.

45 X. Guo, Q. Zhang and H. He, *et al.*, Wastewater flocculation substrate derived three-dimensional ordered macroporous Co single-atom catalyst for singlet oxygen-dominated peroxymonosulfate activation, *Appl. Catal., B*, 2023, 122886, DOI: **10.1016/j.apcatb.2023.122886**.

46 J. Zhang, B. Xin, C. Shan, W. Zhang, D. D. Dionysiou and B. Pan, Roles of oxygen-containing functional groups of O-doped g-C_3N_4 in catalytic ozonation: Quantitative relationship and first-principles investigation, *Appl. Catal., B*, 2021, **292**, 120155, DOI: **10.1016/j.apcatb.2021.120155**.

47 S. Zhao, X. Zhao, S. Ouyang and Y. Zhu, Polyoxometalates covalently combined with graphitic carbon nitride for photocatalytic hydrogen peroxide production, *Catal. Sci. Technol.*, 2018, **8**(6), 1686–1695, DOI: **10.1039/C8CY00043C**.

48 B. Jürgens, E. Irran, J. Senker, P. Kroll, H. Müller and W. Schnick, Melem (2,5,8-Triamino-tri- s -triazine), an Important Intermediate during Condensation of Melamine Rings to Graphitic Carbon Nitride: Synthesis, Structure Determination by X-ray Powder Diffractometry, Solid-State NMR, and Theoretical Studies, *J. Am. Chem. Soc.*, 2003, **125**(34), 10288–10300, DOI: **10.1021/ja0357689**.

49 J. Xu, J. K. Shang, Q. Jiang, Y. Wang and Y. X. Li, Facile alkali-assisted synthesis of g-C_3N_4 materials and their high-performance catalytic application in solvent-free cycloaddition of CO_2 to epoxides, *RSC Adv.*, 2016, **6**(60), 55382–55392, DOI: **10.1039/C6RA10509B**.

50 L. Wang, X. Guo, Y. Chen, S. Ai and H. Ding, Cobalt-doped g-C_3N_4 as a heterogeneous catalyst for photo-assisted activation of peroxymonosulfate for the degradation of organic contaminants, *Appl. Surf. Sci.*, 2019, **467–468**, 954–962, DOI: **10.1016/j.apsusc.2018.10.262**.

51 X. Wang, X. Chen, A. Thomas, X. Fu and M. Antonietti, Metal-Containing Carbon Nitride Compounds: A New Functional Organic-Metal Hybrid Material, *Adv. Mater.*, 2009, **21**(16), 1609–1612, DOI: **10.1002/adma.200802627**.

52 S. M. Youssry, I. S. El-Hallag, R. Kumar, G. Kawamura, A. Matsuda and M. N. El-Nahass, Synthesis of mesoporous Co(OH)2 nanostructure film via electrochemical deposition using lyotropic liquid crystal template as improved electrode materials for supercapacitors application, *J. Electroanal. Chem.*, 2020, **857**, 113728, DOI: **10.1016/j.jelechem.2019.113728**.

53 C. Ding, Z. Gao and J. Wang, *et al.*, The coralline cobalt oxides compound of multiple valence states deriving from flower-like layered double hydroxide for efficient hydrogen generation from hydrolysis of NaBH4, *Int. J. Hydrogen Energy*, 2021, **46**(2), 2390–2404, DOI: **10.1016/j.ijhydene.2020.10.141**.

54 J. Zheng and L. Zhang, Designing 3D magnetic peony flower-like cobalt oxides/g-C_3N_4 dual Z-scheme photocatalyst for remarkably enhanced sunlight driven photocatalytic redox activity, *Chem. Eng. J.*, 2019, **369**(December 2018), 947–956, DOI: **10.1016/j.cej.2019.03.131**.

55 X. Yang, F. Qian and G. Zou, *et al.*, Facile fabrication of acidified g-C_3N_4/g-C_3N_4 hybrids with enhanced photocatalysis performance under visible light irradiation, *Appl. Catal., B*, 2016, **193**, 22–35, DOI: **10.1016/j.apcatb.2016.03.060**.

56 A. El Idrissi, O. Dardari and F. N. N. N. Metomo, *et al.*, Effect of sodium alginate-based superabsorbent hydrogel on tomato growth under different water deficit conditions, *Int. J. Biol. Macromol.*, 2023, **253**, 127229, DOI: **10.1016/j.ijbiomac.2023.127229**.

57 B. El Allaoui, H. Chakhtouna, N. Zari, H. Benzeid, A. el K. Qaiss and R. Bouhfid, Superhydrophobic alkylsilane functionalized cellulose beads for efficient oil/water separation, *J. Water Process. Eng.*, 2023, **54**, 104015, DOI: **10.1016/j.jwpe.2023.104015**.

58 X. Yuan, S. Duan and G. Wu, *et al.*, Enhanced catalytic ozonation performance of highly stabilized mesoporous ZnO doped g-C_3N_4 composite for efficient water decontamination, *Appl. Catal., A*, 2018, **551**, 129–138, DOI: **10.1016/j.apcata.2017.12.011**.

59 B. Babu, J. Shim and K. Yoo, Efficient solar-light-driven photoelectrochemical water oxidation of one-step in-situ synthesized Co-doped g-C_3N_4 nanolayers, *Ceram. Int.*, 2020, **46**(10), 16422–16430, DOI: **10.1016/j.ceramint.2020.03.203**.

60 X. R. Xu and X. Z. Li, Degradation of azo dye Orange G in aqueous solutions by persulfate with ferrous ion, *Sep. Purif. Technol.*, 2010, **72**(1), 105–111, DOI: **10.1016/j.seppur.2010.01.012**.

61 A. Ait El Fakir, Z. Anfar, M. Enneiymy, A. Jada and N. El Alem, Conjugated polymers templated carbonization to design N, S co-doped finely tunable carbon for enhanced synergistic catalysis, *Appl. Catal., B*, 2022, **300**, 120732, DOI: **10.1016/j.apcatb.2021.120732**.

62 L. T. Thao, T. V. Nguyen and V. Q. Nguyen, *et al.*, Orange G degradation by heterogeneous peroxymonosulfate activation based on magnetic $MnFe_2O_4$/α-MnO_2 hybrid, *J. Environ. Sci.*, 2023, **124**, 379–396, DOI: **10.1016/j.jes.2021.10.008**.

63 H. Gao, H. Yang, J. Xu, S. Zhang and J. Li, Strongly Coupled g-C_3N_4 Nanosheets-Co_3O_4 Quantum Dots as 2D/0D Heterostructure Composite for Peroxymonosulfate Activation, *Small*, 2018, **14**(31), 1801353, DOI: **10.1002/smll.201801353**.

64 J. C. Espinosa, P. Manickam-Periyaraman and F. Bernat-Quesada, *et al.*, Engineering of activated carbon surface to enhance the catalytic activity of supported cobalt oxide nanoparticles in peroxymonosulfate activation, *Appl. Catal., B*, 2019, **249**, 42–53, DOI: **10.1016/j.apcatb.2019.02.043**.

65 Q. Li and Q. Wang, Photo(electro)catalyst of Flower-Like Cobalt Oxide Co-Doped g-C_3N_4: Degradation of Methylene Blue under Visible Light Illumination, *Materials*, 2022, **15**(12), 4104, DOI: **10.3390/ma15124104**.

66 R. Yuan, M. Jiang and S. Gao, *et al.*, 3D mesoporous α-$Co(OH)_2$ nanosheets electrodeposited on nickel foam: A new generation of macroscopic cobalt-based hybrid for peroxymonosulfate activation, *Chem. Eng. J.*, 2020, **380**, 122447, DOI: **10.1016/j.cej.2019.122447**.

67 Y. Yao, C. Xu, S. Miao, H. Sun and S. Wang, One-pot hydrothermal synthesis of Co(OH)2 nanoflakes on graphene sheets and their fast catalytic oxidation of phenol in liquid

phase, *J. Colloid Interface Sci.*, 2013, **402**, 230–236, DOI: 10.1016/j.jcis.2013.03.070.

68 P. T. Babar, A. C. Lokhande and B. S. Pawar, *et al.*, Electrocatalytic performance evaluation of cobalt hydroxide and cobalt oxide thin films for oxygen evolution reaction, *Appl. Surf. Sci.*, 2018, **427**, 253–259, DOI: 10.1016/j.apsusc.2017.07.142.

69 M. Xie, J. Tang and L. Kong, *et al.*, Cobalt doped g-C_3N_4 activation of peroxymonosulfate for monochlorophenols degradation, *Chem. Eng. J.*, 2019, **360**, 1213–1222, DOI: 10.1016/j.cej.2018.10.130.

70 Y. Wang, L. Fang, Z. Wang and Q. Yang, Peroxymonosulfate activation by graphitic carbon nitride co-doped with manganese, cobalt, and oxygen for degradation of trichloroethylene: Effect of oxygen precursors, kinetics, and mechanism, *Sep. Purif. Technol.*, 2021, **278**, 119580, DOI: 10.1016/j.seppur.2021.119580.

71 T. Ma, Y. Wu, N. Liu, X. Tao and Y. Wu, Iron-doped g-C_3N_4 modified $CoMoO_4$ as an efficient heterogeneous catalyst to activate peroxymonosulfate for degradation of organic dye, *J. Dispersion Sci. Technol.*, 2022, **43**(1), 80–93, DOI: 10.1080/01932691.2020.1817060.

72 Q. Qin, X. Gao, X. Wu and Y. Liu, NaBH4-treated cobalt-doped g-C_3N_4 for enhanced activation of peroxymonosulfate, *Mater. Lett.*, 2019, **256**, 126623, DOI: 10.1016/j.matlet.2019.126623.

73 X. Yu, X. Wu, F. Guo, J. Liu and Q. Zhao, Visible-light-assisted activation of peroxymonosulfate (PMS) over CoO_x@C/g-C_3N_4 composite for efficient organic pollutant degradation, *J. Alloys Compd.*, 2023, **948**, 169702, DOI: 10.1016/j.jallcom.2023.169702.

74 X. Zhang, B. Xu and S. Wang, *et al.*, Tetracycline degradation by peroxymonosulfate activated with CoNx active sites: Performance and activation mechanism, *Chem. Eng. J.*, 2022, **431**, 133477, DOI: 10.1016/j.cej.2021.133477.

75 Q. Yang, J. An, Z. Xu, S. Liang and H. Wang, Performance and mechanism of atrazine degradation using Co_3O_4/g-C_3N_4 hybrid photocatalyst with peroxymonosulfate under visible light irradiation, *Colloids Surf., A*, 2021, **614**, 126161, DOI: 10.1016/j.colsurfa.2021.126161.

76 Y. Hu, Z. Zhao, H. Dai and W. Zhou, Promoted generation of singlet oxygen by oxygen vacancies-enriched Co_3O_4/g-C_3N_4 catalyst for efficient degradation of phenanthrene, *Colloids Surf., A*, 2023, **662**, 130958, DOI: 10.1016/j.colsurfa.2023.130958.

77 X. Guo, S. Ai, D. Yang, L. Zhao and H. Ding, Synergistic photocatalytic and Fenton-like degradation of organic contaminants using peroxymonosulfate activated by $CoFe_2O_4$ @ g -C_3N_4 composite, *Environ. Technol.*, 2021, **42**(14), 2240–2253, DOI: 10.1080/09593330.2019.1697378.

78 C. Yue, J. Jiang and M. Li, *et al.*, Accelerating the peroxymonosulfate activation and charge transfer by construction of Fermi energy level-matched $CoWO_4$/g-C_3N_4 photocatalyst for typical antibiotics degradation, *Sep. Purif. Technol.*, 2022, **301**, 122020, DOI: 10.1016/j.seppur.2022.122020.

79 T. B. Nguyen, C. P. Huang, R. A. Doong, M. H. Wang, C. W. Chen and C. D. Dong, Manipulating the morphology of 3D flower-like $CoMn_2O_4$ bimetallic catalyst for enhancing the activation of peroxymonosulfate toward the degradation of selected persistent pharmaceuticals in water, *Chem. Eng. J.*, 2022, **436**, 135244, DOI: 10.1016/j.cej.2022.135244.

80 Y. Ding, L. Zhu, N. Wang and H. Tang, Sulfate radicals induced degradation of tetrabromobisphenol A with nanoscaled magnetic $CuFe_2O_4$ as a heterogeneous catalyst of peroxymonosulfate, *Appl. Catal., B*, 2013, **129**, 153–162, DOI: 10.1016/j.apcatb.2012.09.015.

81 G. V. Buxton, C. L. Greenstock, W. P. Helman and A. B. Ross, Critical Review of rate constants for reactions of hydrated electrons, hydrogen atoms and hydroxyl radicals OH/$^{\bullet}O^{-}$ in Aqueous Solution, *J. Phys. Chem. Ref. Data*, 1988, **17**(2), 513–886, DOI: 10.1063/1.555805.

82 P. Neta, R. E. Huie and A. B. Ross, Rate Constants for Reactions of Inorganic Radicals in Aqueous Solution, *J. Phys. Chem. Ref. Data*, 1988, **17**(3), 1027–1284, DOI: 10.1063/1.555808.

83 P. S. Rao and E. Hayon, Redox potentials of free radicals. IV. Superoxide and hydroperoxy radicals. O_2- and. HO_2, *J. Phys. Chem.*, 1975, **79**(4), 397–402, DOI: 10.1021/j100571a021.

84 T. A. Dahl, W. R. Midden and P. E. Hartman, Some prevalent biomolecules as defenses against singlet oxygen damage, *Photochem. Photobiol.*, 1988, **47**(3), 357–362, DOI: 10.1111/j.1751-1097.1988.tb02737.x.

85 Z. Fang, J. Qi and Y. Xu, *et al.*, Promoted generation of singlet oxygen by hollow-shell CoS/g-C_3N_4 catalyst for sulfonamides degradation, *Chem. Eng. J.*, 2022, **441**, 136051, DOI: 10.1016/j.cej.2022.136051.

86 X. Li, L. Wu, A. Zhang, S. Wu, Y. Lin and C. Yang, Cobalt doping amount determines dominant reactive species in peroxymonosulfate activation via porous carbon catalysts co-doped by cobalt and nitrogen, *J. Environ. Sci.*, 2024, **138**, 212–226, DOI: 10.1016/j.jes.2023.03.038.

87 J. Ye, D. Yang, J. Dai, C. Li, Y. Yan and Y. Wang, Strongly coupled cobalt/oxygen co-doped porous g-C_3N_4 heterostructure with abundant oxygen vacancies modulated the peroxymonosulfate activation pathway, *Chem. Eng. J.*, 2022, **431**, 133972, DOI: 10.1016/j.cej.2021.133972.

88 Y. Yu, N. Li and X. Lu, *et al.*, Co/N co-doped carbonized wood sponge with 3D porous framework for efficient peroxymonosulfate activation: Performance and internal mechanism, *J. Hazard. Mater.*, 2022, **421**, 126735, DOI: 10.1016/j.jhazmat.2021.126735.

89 L. Gao, Z. Li and W. Yi, *et al.*, Effective Pb^{2+} adsorption by calcium alginate/modified cotton stalk biochar aerogel spheres: With application in actual wastewater, *J. Environ. Chem. Eng.*, 2023, **11**(1), 109074, DOI: 10.1016/j.jece.2022.109074.

90 C. Li, J. Wu, W. Peng, Z. Fang and J. Liu, Peroxymonosulfate activation for efficient sulfamethoxazole degradation by $Fe3O_4$/β-FeOOH nanocomposites: Coexistence of radical and non-radical reactions, *Chem. Eng. J.*, 2019, **356**, 904–914, DOI: 10.1016/j.cej.2018.09.064.

91 X. Luo, L. Bai and J. Xing, *et al.*, Ordered Mesoporous Cobalt Containing Perovskite as a High-Performance Heterogeneous Catalyst in Activation of Peroxymonosulfate, *ACS Appl. Mater. Interfaces*, 2019, **11**(39), 35720–35728, DOI: **10.1021/acsami.9b11322**.

92 C. Gong, F. Chen and Q. Yang, *et al.*, Heterogeneous activation of peroxymonosulfate by Fe–Co layered doubled hydroxide for efficient catalytic degradation of Rhoadmine B, *Chem. Eng. J.*, 2017, **321**, 222–232, DOI: **10.1016/j.cej.2017.03.117**.

93 F. Liu, J. Cao and Z. Yang, *et al.*, Heterogeneous activation of peroxymonosulfate by cobalt-doped MIL-53(Al) for efficient tetracycline degradation in water: Coexistence of radical and non-radical reactions, *J. Colloid Interface Sci.*, 2021, **581**, 195–204, DOI: **10.1016/j.jcis.2020.07.100**.

94 A. Amjlef, A. Ait El Fakir and S. Farsad, *et al.*, Efficient degradation of orange G dye using the quartz-sand@polythiophene composite for peroxymonosulfate activation: a sustainable approach for advanced oxidation processes, *Mater Adv.*, 2023, DOI: **10.1039/D3MA00596H**.